Integrated Turbine Component Cooling Designs Facilitated by Additive Manufacturing and Optimization

Final Report

September 1, 2019 – December 31, 2023

Report issued April 12, 2024

Submitted to:

Department of Energy (DOE)
Office of Fossil Energy, Advanced Turbine Program

DOE Award Number: DEFE0031760

Principal Investigator: David G. Bogard, University of Texas at Austin
Email: dbogard@mail.utexas.edu, Phone: 512-471-3128
Co-Principal Investigator: Todd Oliver, University of Texas at Austin
Co-Principal Investigator: Karen A. Thole, Pennsylvania State University

Submitting organizations:

Turbulence and Turbine Cooling Research Laboratory (TTCRL)
Walker Department of Mechanical Engineering
University of Texas at Austin
204 E. Dean Keeton Street; Stop C2200
Austin, TX 78712

DUNS# 170230239

Steady Thermal Aero Research Turbine (START) Laboratory
Department of Mechanical Engineering
Pennsylvania State University
University Park, PA 16802

Signature of PI: 

Integrated Turbine Component Cooling Designs Facilitated by Additive Manufacturing and Optimization

Executive Summary

This research program involved the development of improved gas turbine cooling by optimizing the combined internal and film cooling configurations used for turbine blades and vanes. Improved cooling of turbine airfoils allows the gas turbines to be operated at higher temperatures which improves efficiency for gas turbine-based power generation. This also facilitates operation with hydrogen-based fuels which inherently generate higher operating temperatures. Designs of the new cooling configurations were based on the added geometric flexibility that is available when using metal additive manufacturing techniques. When making these designs, adjustments were made to account for imperfections occurring in the metal additive manufacturing process. New designs for film cooling holes were developed using computational adjoint gradient optimization techniques which generated a unique film cooling hole with 70% greater film cooling effectiveness compared to conventional shaped film cooling holes. A major factor in improving the film cooling effectiveness were small external protrusions on either side of the new hole which generated vortices that pushed coolant towards the surface and increased the lateral spreading of the coolant. Our studies also included optimization of film cooling holes that can be built with conventional manufacturing techniques and optimizing the internal coolant channels that supply coolant to the film cooling holes. Various internal coolant channel shapes were investigated and designs that maximized the cooling of the airfoil while minimizing pressure losses in the channel flows were identified. Testing and verification of the performance of the final configurations was done with a transonic wind tunnel facility which allowed testing at engine realistic high velocities. Final testing of the combined internal and film cooling configurations was done by incorporating the configurations in Penn State's National Experimental Turbine (NExT) vane. These tests confirmed the enhanced overall cooling effectiveness provided by the new cooling configuration designs.

Summary of Results for the Nine Tasks completed in this project:

Task 1 (UT) – Optimize internal cooling channels coupled with film cooling using RANS.

The initial phase of this project was to develop improved film cooling holes optimized for performance with a crossflow internal channel that is typical for turbine blades. The optimized internal channel with film cooling holes would take advantage of the flexibility in geometries possible with additive manufacturing. These designs were initially developed computationally and then verified experimentally. All computational work was done using the ANSYS Fluent RANS code. There were three phases to this work: a. evaluation of the improved film cooling performance possible with a rounded inlet, b. a parametric evaluation of the effects of lateral and forward expansion angles for a fan shaped hole, and c. optimization of the complete hole geometry using adjoint optimization techniques. These studies, presented in detail in Jones et al., (2021 (a) and (b)) and Jones et al. (2023), are summarized below.

The initial study examined the effect of rounding the inlet of a standard 7-7-7 shaped film cooling hole[1] on the film cooling performance and is presented in detail in Jones et al. (2023). As shown in Fig. 1.1, film cooling holes manufactured with conventional techniques have sharp inlets to film cooling holes. The sharp corners inherently cause separation of the coolant flow entering the hole leading to inefficient diffusing of the coolant towards the exit of the hole, resulting in lower adiabatic effectiveness. Using additive manufacturing, various hole inlet geometries can be constructed that might be expected to improve film cooling performance. Two concepts were evaluated, a rounded inlet, shown in Fig. 1.1, and a swept inlet design. Both these designs were evaluated using computational predictions and experimental measurements. In this study, a row of film cooling holes fed by a crossflow channel was used. Previous studies showed that the film cooling performance was sensitive to the velocity in the coolant channel relative to the mainstream velocity, VR_c, and the coolant jet velocity relative to the mainstream velocity, VR. Consequently, computational predictions and experimental measurements were done for VR_c = 0.2 to 0.6 and VR = 0.5 to 1.7. Representative results from the computational predictions and experimental tests done at VR_c = 0.4 are shown in Fig. 1.2. These results showed that both inlet designs were successful in increasing adiabatic effectiveness by as much as 50%. There were significant differences between the computational predictions and the experimental measurements. This was expected since RANS computational predictions have difficulties in predicting the diffusion of coolant flows for film cooling. However, the computations were consistent with the experiments in predicting better performance for the modified film cooling hole inlets.

The second phase of this study was to conduct a parametric study of laidback, fan shaped holes to determine the optimum lateral and forward expansion angles. This study is presented in detail in Jones et al. (2021 (a)). Initially, computational predictions were made for 53 different

[1] Schroeder and Thole, J. of Turbomachinery (2022)

hole geometries operating over a range of 5 coolant jet to mainstream velocity ratios, resulting in 265 geometry and operating conditions simulated. The film cooling holes had rounded inlets and a range of lateral and forward expansion angles from 1° to 18°. The nomenclature used to define the expansion angles used for each hole was L_L-L_R-F, where L_L was the left-side lateral angle, L_R was the right-side lateral angle, and F was the forward angle.

To evaluate the adiabatic effectiveness performance, the spatially averaged adiabatic effectiveness, η_{SA}, was normalized using the ratio of the coverage width, t, to the pitch between holes, P, i.e. η_{SA}/(t/P). Using this normalization accounts for the possibility of the use of a closer lateral hole spacing resulting in increased adiabatic effectiveness. In order to make comparisons in terms of equal coolant mass flow rates per unit width of the surface, the coolant velocity ratio was also normalized with the (t/P) ratio as: $VR/(t/P)$. As shown in Fig. 1.3, the results from this parametric study showed that the 15-15-1 hole had the maximum adiabatic effectiveness performance which occurred at the maximum coolant velocity ratio of VR = 1.7 that was computed. Four hole geometries were selected for validation with experimental measurements: 3-3-1, 7-7-7, 12-12-6, and 15-15-1. The experimental results confirmed relative performance computationally predicted for each of these hole geometries, although the computational predictions were noticeably higher than measured values for VR >1. Note that the experimentally measured adiabatic effectiveness for the 15-15-1 hole was 40% higher than for the extensively studied 7-7-7 hole.

The third phase of this task was to use adjoint optimization techniques to modify film cooling hole geometries to improve film cooling performance. This study is presented in detail in Jones et al. (2021 (b)). The adjoint optimization was initiated with the RANS computational simulations of the 15-15-1 hole. The adjoint gradient process modified the hole and surrounding surface geometry with an objective function to maximize area averaged adiabatic effectiveness downstream of the film cooling hole for a coolant jet velocity ratio of VR = 1.67 and a coolant channel velocity ratio of VR_c = 0.4. Two coolant channel orientations were used, a crossflow feed and a co-flow feed. The hole geometries generated by these adjoint optimization processes, the X-AOpt hole for crossflow fed and the Co-AOpt hole for co-flow fed, are shown in Fig.1.5. Also shown in Figure 1.5 for reference are schematics for the 7-7-7 SI and the 15-15-1 RI holes where “SI” refers to a sharp inlet and “RI” refers to a rounded inlet. The internal geometry for these holes remained similar to the 15-15-1 RI hole, but protrusions were developed primarily to the external surface upstream and to the sides of the hole exit. The computationally predicted area averaged adiabatic effectiveness for these holes, over the range x/D = 5 to 20, are shown in Fig. 1.6. For comparison, also shown in Fig. 1.6 are experimentally measured area averaged adiabatic effectiveness for the X-AOpt and 15-15-1 RI holes. Most noticeable in Fig. 1.6 is that the computational predictions of η_{SA} are much larger than the experimental measurements for the X-AOpt hole, but the experimental measurements for η_{SA} the X-AOpt hole are still larger than that for the 15-15-1 hole, with the maximum η_{SA} value about 30% larger for the X-AOpt hole compared to the 15-15-1 hole. Based on these results, the X-AOpt hole was selected as the

optimum film cooling hole geometry and was thoroughly tested as described in other tasks completed in our experimental program.

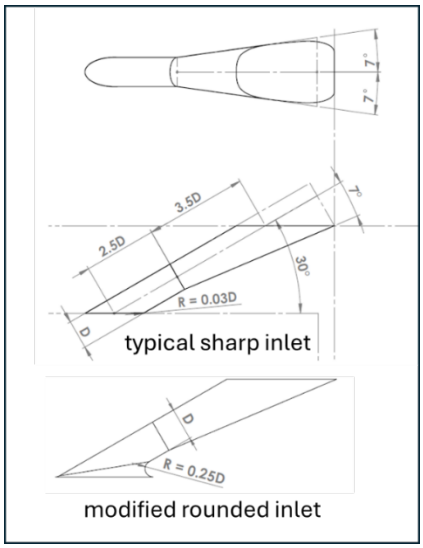

Figure 1.1. Schematic showing the rounding of film cooling hole inlet.

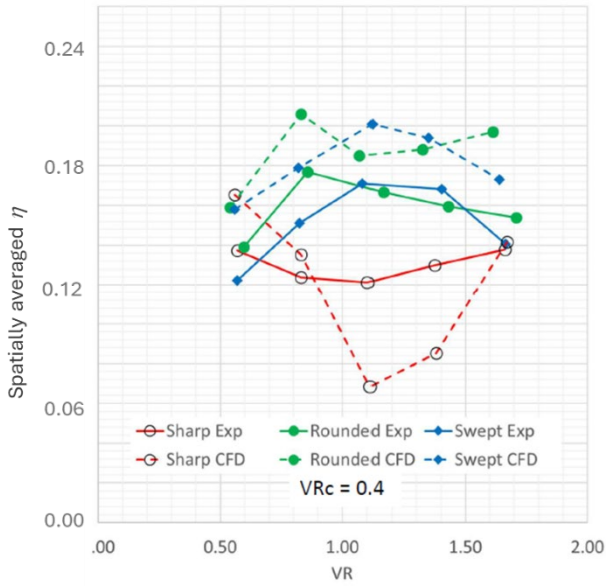

Figure 1.2. Experimental and computational adiabatic effectiveness values for varying *VR* and VR_c = 0.4.

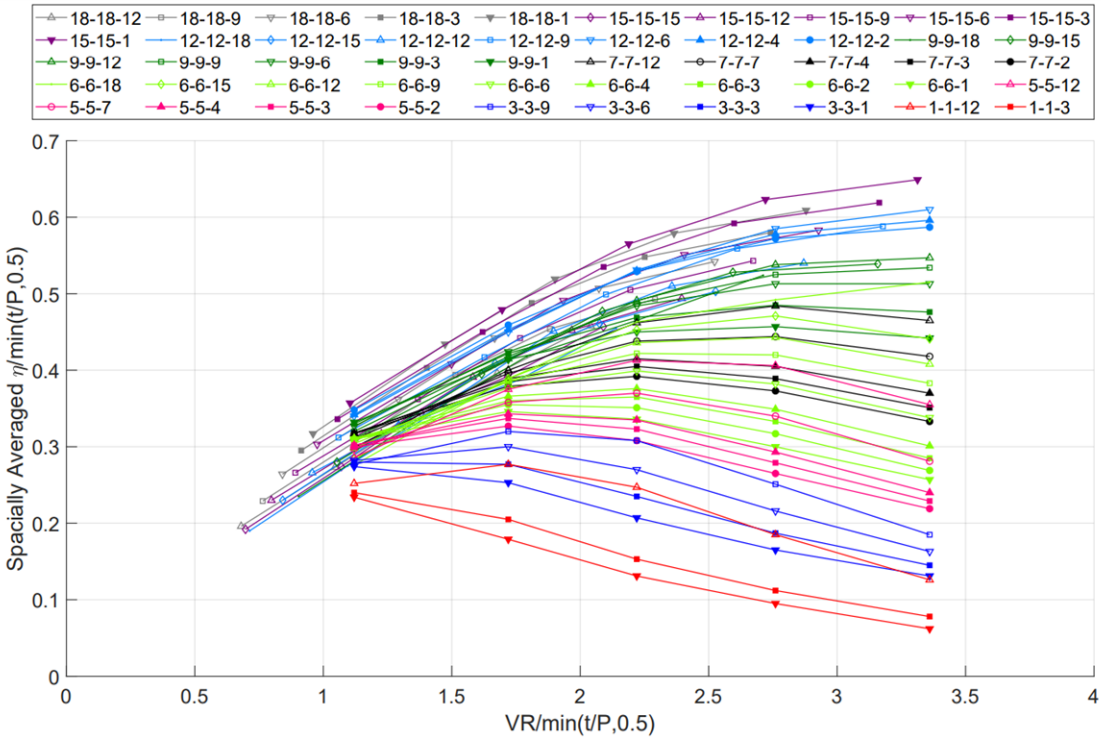

Figure 1.3. Computational predictions of the normalized spatial average adiabatic effectiveness with varying lateral and forward expansion angles.

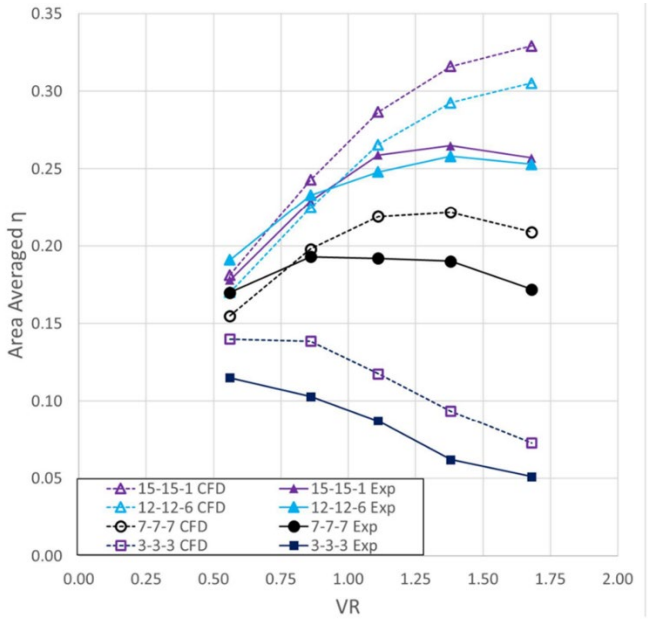

Figure 1.4. Computational predictions and experimental measurements of the spatially averaged adiabatic effectiveness for four hole geometries: 15-15-1, 12-12-6, 7-7-7, and 3-3-3.

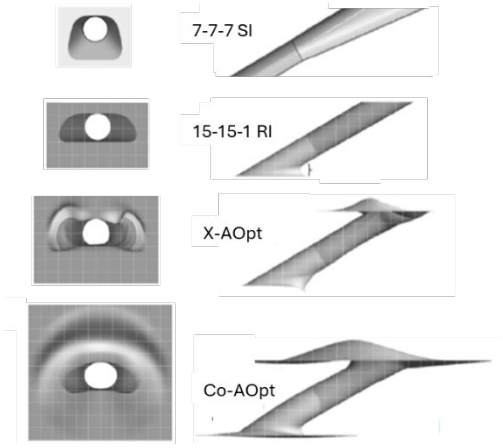

Figure 1.5. Schematics of the adjoint optimized holes X-AOpt and Co-AOpt. Also shown for reference are the 7-7-7 SI and 15-15-1 RI holes.

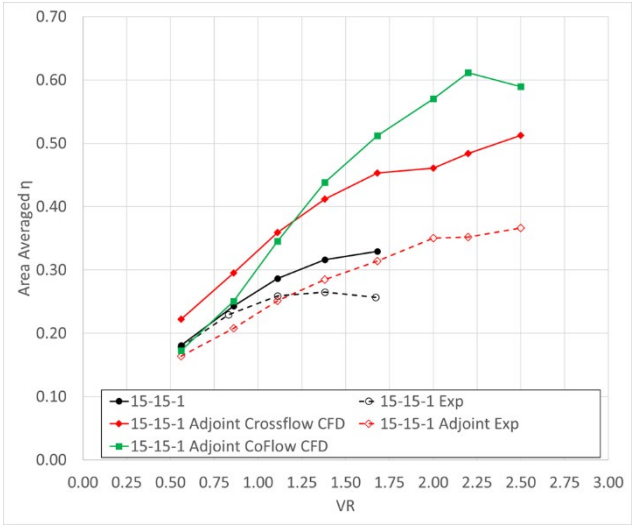

Figure 1.6. Computational and experimental area averaged adiabatic effectiveness for the X-AOpt and Co-AOpt holes. Also shown for reference is the performance of the 15-15-1 RI hole.

Task 2 (PSU) – Printing of the AM optimized coupons at 1X scale with a combined cooling channel supply and film-cooling hole.

The research question for this task addressed the ability to additively manufacture specific features on engine scale film cooling holes with current AM capabilities and whether these features improve the overall cooling effectiveness. Four cooling hole shapes were printed involving two basic diffuser shapes with variations of fillet radii for the holes. These hole shapes were derived and previously reported by prior optimization studies. The research results from this task were reported by Veley, et al. (2023) and will be summarized in this section of the report.

A summary of the holes chosen and resulting printability of the challenging film-cooling holes is shown in Figures 2.1 and 2.2. The data in Fig. 2.2 indicate fairly good agreement between the as-built and the design intent surfaces; however, there are deviations derived from the AM resolution, which impacts the hole size, tolerancing on the expansion angles, and the fillets on inlets and exits.

Figure 2.3 shows contours of the local augmentation of overall effectiveness for all four hole shapes at three blowing ratios (M=1.5, 2, and 3). Immediately evident from Fig. 2.3 is that the cooling uniformity for the 15-15-1 holes is more two-dimensional (more uniform coverage) than the 9-9-3 holes. Also apparent is that the augmentation in effectiveness increases with blowing ratios regardless of cooling hole shape. For both the 9-9-3 RI and the 9-9-3 RIE there are noticeable variations in effectiveness between the different holes for the same geometry, as shown in Figs. 2.3(a) and 2.3(b), which can be attributed to manufacturing variations from AM. In all, this study showed that AM roughness features cause variations in inlet rounding, which impacts the overall effectiveness.

In terms of printing, because the film cooling holes were printed in an orientation with the metering axis perpendicular to the substrate, the cross-sectional areas and hydraulic diameters of the cooling holes were slightly larger than the design intent. The holes with inlet fillets also contained inlet roughness features that occur because of the overhang distances during the build to create the leeward side of the hole. The results indicated that although the as-built sharp inlet caused the highest in-hole convection, the sharp inlet resulted in more film mixing downstream than holes with fillets at the inlet or exit of the hole. Therefore, it is important for designers to understand how the as-built hole design impacts the cooling mechanisms which in turn impact the overall performance of AM film cooling holes.

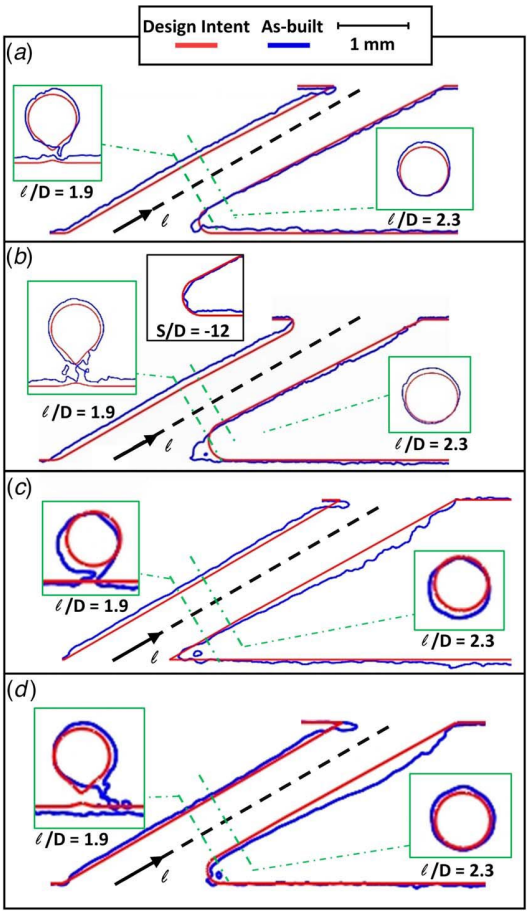

Fig. 2.1 Cross sections of CT scanned as-built (blue) and best-fit design intent (red) of the (a) 9-9-3 RI, (b) 9-9-3 RIE, (c) 15-15-1 SI, and (d) 15-15-1 RI holes

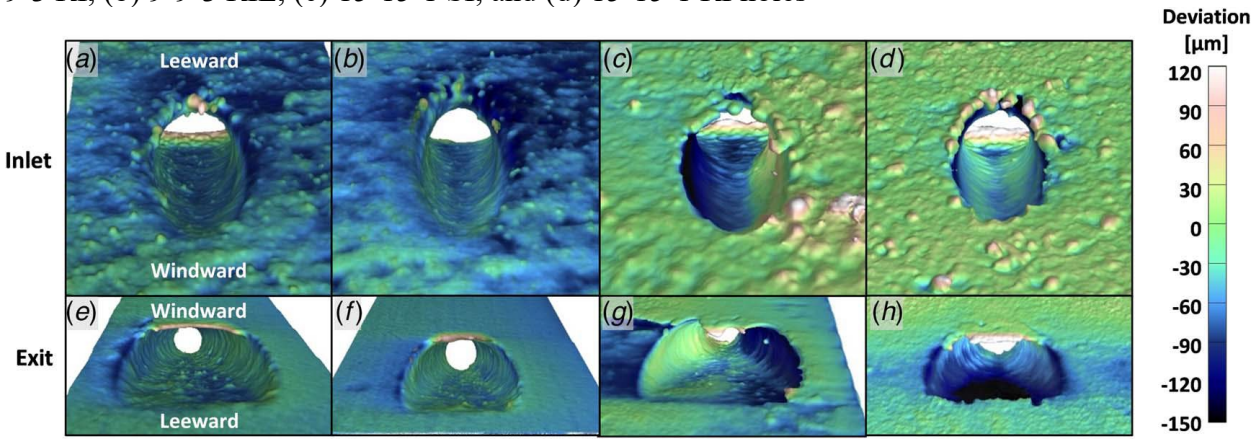

Fig. 2.2 Local deviations from the best-fit design intent of a single hole from each geometry: (a), (e) 9-9-3 RI, (b), (f) 9-9-3 RIE, (c), (g) 15-15-1 SI, and (d), (h) 15-15-1 RI. The view of the inlets (a)–(d) shows the dross roughness features.

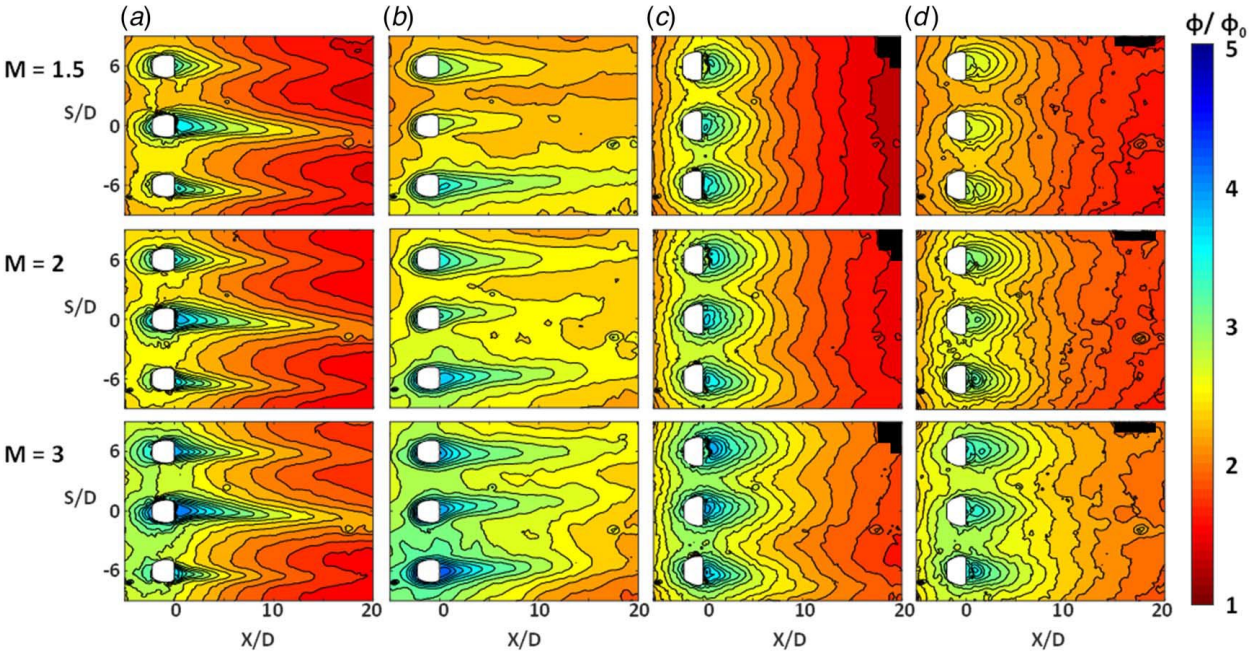

Fig. 2.3 Contours of the augmentation in cooling effectiveness at M=1.5, 2.0, and 3.0 for the (a) 9-9-3 RI, (b) 9-9-3 RIE, (c) 15-15-1 SI, and (d) 15-15-1 RI. Black regions are the location of surface thermocouples and were not included in averages.

Task 3 (PSU) – Testing of AM print optimized coupons at 1X scale to characterize bulk heat transfer coefficients (h) and pressure losses (f) with co-flow, counter-flow, and cross-flow supplies.

This task aimed to provide additional experimental pressure loss and heat transfer measurements for a range of different channel shapes that have not been evaluated in the literature. Additionally, this paper addresses the scaling of friction factor and Nusselt number results with a characteristic length scale other than hydraulic diameter for polygonal-shaped channels (Wildgoose and Thole, 2023). The follow-on work was to assess how these channel shapes impacted the film-cooling performance (Veley, et al., 2023).

To assess the impact channel shape has on the pressure loss and convective heat transfer, a variety of straight channel shapes were fabricated using direct metal laser sintering (DMLS). Nine channel shapes were selected for evaluation and are specified in Table 1. The nine channel shapes were designed to maintain the same cross-sectional perimeter and coupon length to guarantee the same convective heat transfer surface area. The design perimeter for each channel was chosen to match a circular diameter of 1.5 mm giving a perimeter of 4.8 mm. Each test coupon was designed to have nine channels. The channel pitch spacing (S) was controlled such that the fin efficiency between channels was greater than 95% to fulfill the constant surface temperature boundary condition during heat transfer measurements. The length-to-hydraulic diameter ratios of the channels were between $33 < L/D_h < 54$, which meets fully developed conditions.

Results from this study include the augmentations of Nusselt number and friction factor relative to smooth correlations shown in Figure 3.1. The ellipse, diamond, circle, hexagon, and pentagon exhibited lower friction factor augmentation for an identical Nusselt augmentation compared to the rectangle and triangle. Nusselt number and friction factor augmentations for all the channel shapes are between the square and diamond shapes, signifying that roughness and surface deformations are significant contributors to friction factor and Nusselt number augmentation. The ellipse, hexagon, circle, diamond, and pentagon contain the same Nusselt number augmentation as the rectangle and triangle for a lower pressure drop penalty at a given Reynolds number. The pentagon contains the same Nusselt number augmentation as the triangle even though the pentagon has a 21% lower friction factor at the same Reynolds numbers.

Table 1 Geometric specifications for coupons sharing a constant perimeter (P_{des} = 4.79 mm)

Coupon Name	$D_{h,act}$ (μm)	$A_{c,act}$ (μm^2) · 10^7	$\frac{D_{h,act}}{D_{h,des}}$	$\frac{p_{act}}{p_{des}}$	$\frac{A_{c,act}}{A_{c,des}}$	$\frac{S_{des}}{D_{h,des}}$	$\frac{R_a}{D_{h,act}}$	Geometry aspect ratios (μm)	
Circle	1590	1.81	1.04	1.06	1.10	1.43	0.0074	$a = D_h$	
Hexagon	1497	1.68	1.08	1.04	1.13	1.57	0.0037	a = 797.96	
Pentagon	1428	1.60	1.08	1.04	1.13	1.66	0.0048	a = 957.56	
Ellipse	1340	1.51	1.05	1.05	1.09	1.66	0.0049	a/b = 2	
Diamond	1314	1.46	1.10	1.03	1.13	1.84	0.0037	a/b = 1	
Square	1283	1.50	1.07	1.09	1.17	1.80	0.0133	a/b = 1	
Rectangle	1200	1.34	1.13	1.04	1.17	1.99	0.0060	a/b = 2	
Trapezoid	1145	1.32	1.11	1.07	1.19	2.16	0.0148	a/b = 0.8 Θ = 60 deg	
Triangle	1047	1.19	1.14	1.05	1.20	2.38	0.0114	Θ = 60 deg	

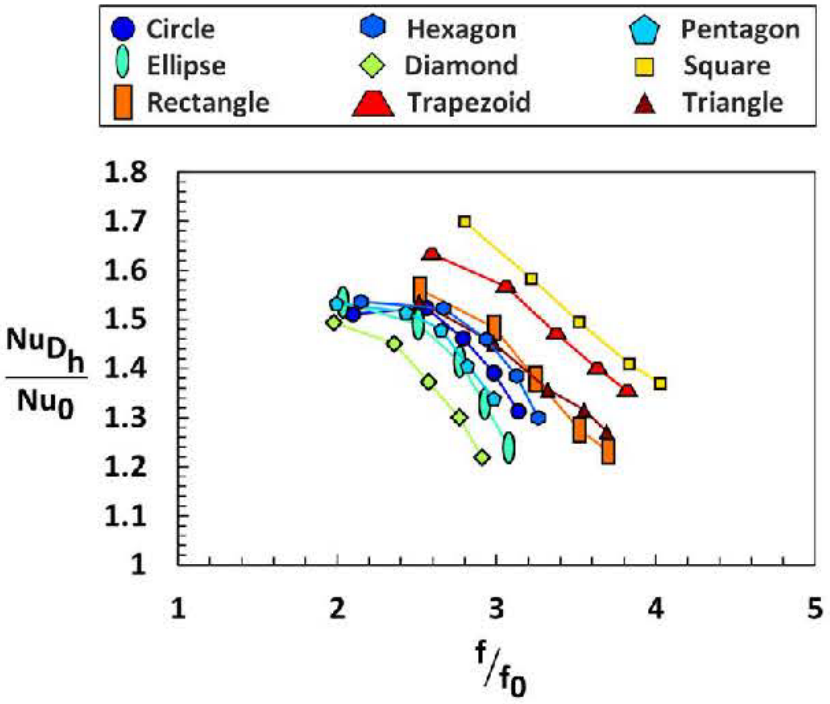

Fig. 3.1 Nusselt number and friction factor augmented by a hydraulically smooth channel for the different channel shapes over a range of fully turbulent Reynolds numbers

Beyond the measurements of internal heat transfer coefficients, these channel geometries were further explored to understand the impacts of the supply channel on the external film cooling. As such, the 7-7-7 film cooling hole geometry was integrated into coupons with each hole having a single supply channel with the channel shape mirroring those in Table 1. The results from these tests are shown in in Fig. 3.2 (Veley and Thole, 2023)

Fig. 3.2(a-j) shows contours of the overall effectiveness from the experiments for all ten channel shapes. From these contours, the circle channel feed resulted in the lowest cooling effectiveness whereas the trapezoid and the triangle – vertex up showed the highest cooling. As noted in Table 1 the circle also has the largest cross-sectional area while the trapezoid and triangles have the smallest cross-sectional areas of the tested geometries. The average velocity through each channel is inversely related to the cross-sectional area because the internal channel Reynolds number is maintained for all of these shapes. Consequently, the circle has the lowest average velocity through the supply channels, whereas the trapezoid and triangles have the highest average velocity of all the channels. These variations in velocity affect the internal heat transfer coefficient; however, the secondary flows also affect the heat transfer coefficient. The corners of the non-circular channels have a reduction in the heat transfer from the edges of the channel, thereby reducing the average heat transfer coefficient. The average internal heat transfer coefficients from CFD predictions were used to calculate the fin efficiency of the walls between the channels. Of the five shapes, the triangle – vertex up and triangle – vertex down had the highest fin efficiencies at 0.84 and 0.85, respectively; the square had the lowest fin efficiency at 0.80. These high fin efficiencies indicate that the walls between the channels were able to conduct the heat from the external surface to the bottom surfaces of the supply channels, which had a major effect on the film-cooling as well.

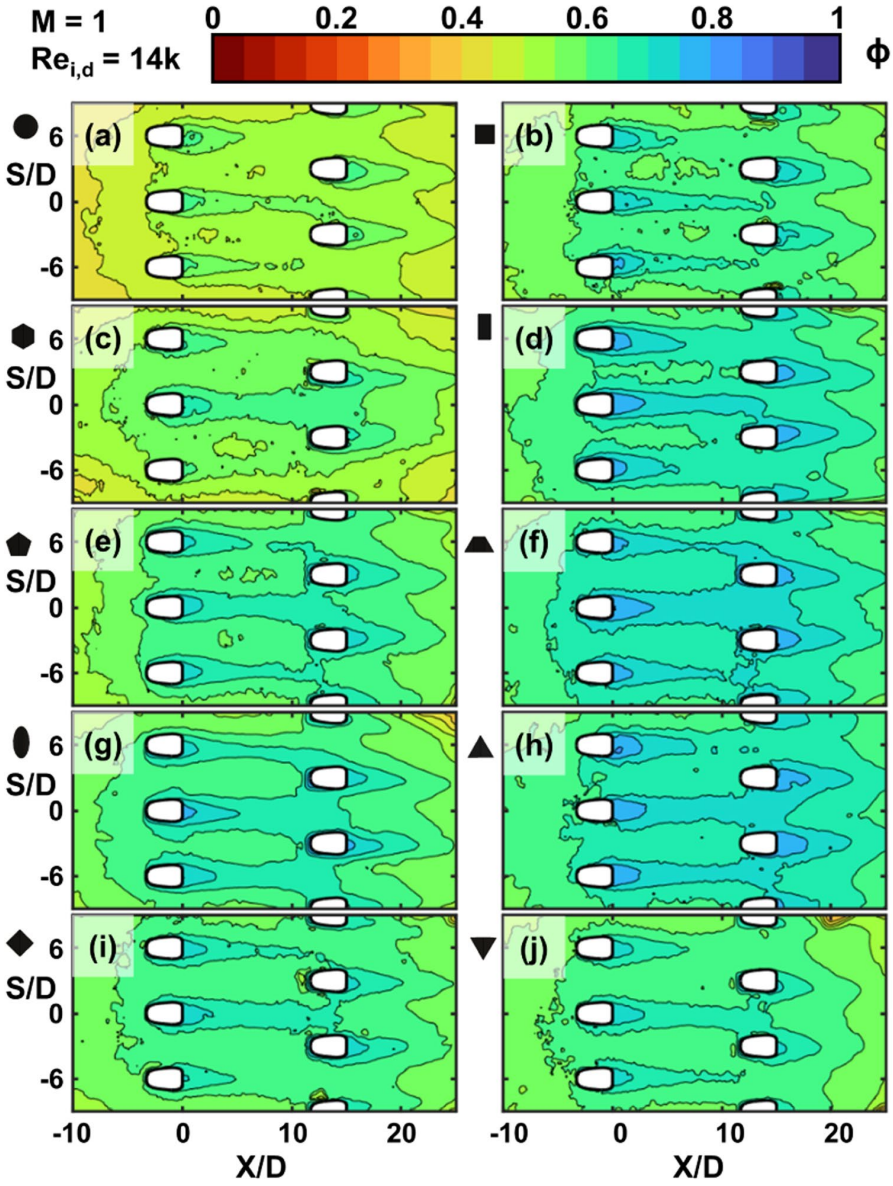

Fig. 3.2. Overall effectiveness contours at M = 1 and Rei,d = 14k for the (a) Circle, (b) Square, (c) Hexagon, (d) Rectangle, (e) Pentagon, (f) Trapezoid, (g) Ellipse, (h) Triangle – Vertex Up, (i) Diamond, and (j) Triangle – Vertex Down.

Ribs within internal channels were also found to be an important impact on the cooling as was shown by (Veley, et al., 2024) as shown in Figure 3.3. The region averaged was $-9 \leq S/D \leq 9$ and $-5 \leq X/D \leq 10$, which is the coverage area of the center three first-row holes, and only extends to the start of the second row of holes for the cases that have a second row. To show the area-average trend of the baselines, ϕ_0 was included for M=0 (no film-cooling). The individual channels have an overall cooling effectiveness that is 80% higher than that of the single channel. In fact, the results in Fig. 3.3 show that in order to obtain an overall effectiveness equivalent to the baseline effectiveness on the non-ribbed individual channels without film cooling, the non-ribbed single channel has to pass enough coolant through the cooling holes to set M=1 (ϕ = 0.36). Therefore, the same effectiveness can be obtained from a supply channel with superior

cooling performance but without film cooling as can be obtained from a supply channel with poor internal cooling performance that has the added benefit of film cooling.

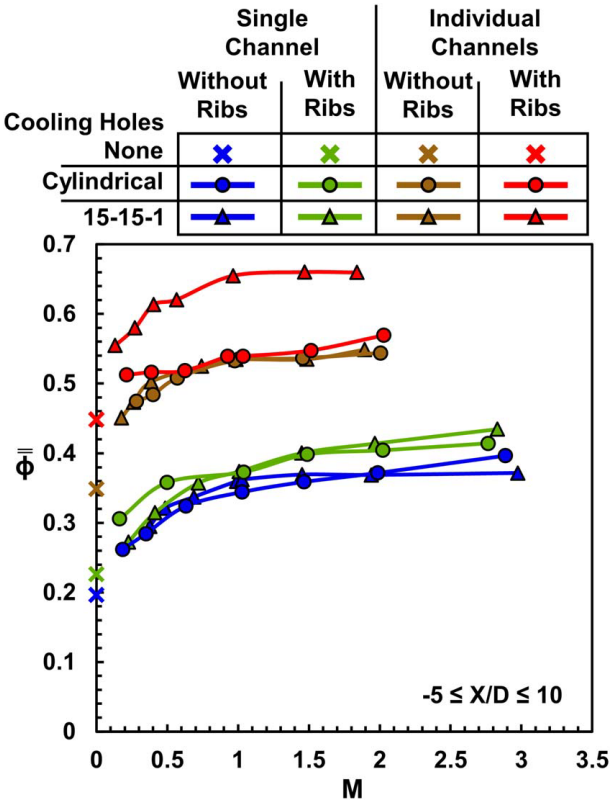

Fig. 3.3 Area-averaged overall cooling effectiveness across several blowing ratios of the first row of holes (−5≤X/D≤10) for all geometries.

Task 4 (UT) – Wind tunnel studies with 5X coupons with and without AM roughness simulations.

The UT low speed wind tunnel facility was modified to incorporate an internal coolant flow channel that ran parallel to the mainstream flow with coolant velocities typical of actual engine conditions. As described in Horner et al. (2022), this new test section has the capability of measuring adiabatic effectiveness and overall cooling effectiveness by using two different test surfaces. The coolant channel was operated over a range of coolant channel to mainstream velocity ratios of VR_c = 0.2 to 0.4. Measurements were made of the adiabatic effectiveness for the X-AOpt, Co-AOpt, 15-15-1 RI, and 7-7-7 SI holes over a range of film cooling jet velocity ratios were presented in Gutierrez et al. (2022). Results from these measurements, shown in Fig. 4.1, are presented in terms of spatially averaged adiabatic effectiveness, η_{SA}, for varying coolant jet velocity ratios, VR = 0.5 to 3.4, at a channel velocity ratio of VR_c = 0.2. These results show that the adiabatic effectiveness for the X-AOpt hole is 75% larger than for the baseline 7-7-7 SI hole and 25% larger than for the parametrically optimized 15-15-1 RI hole.

Overall cooling effectiveness measurements were made for the 15-15-1 RI and X-AOpt holes using the 5X scale models at UT and the 1X scale models (built with metal AM) at PSU. Results from these tests are presented in Fig. 4.2 in terms of the overall cooling effectiveness augmentation, $\bar{\bar{\phi}}/\phi_0$, where $\bar{\bar{\phi}}$ is the spatially averaged overall cooling effectiveness with film cooling and ϕ_0 is the overall cooling effectiveness without film cooling. Consequently, the $\bar{\bar{\phi}}/\phi_0$ parameter gives an indication of the increase in overall cooling effectiveness due to the addition of film cooling relative to overall cooling effectiveness with internal cooling alone. All film cooling holes provided significant increases in overall cooling effectiveness, with maximum improvement occurring with the X-AOpt holes. The 1X holes had greater relative roughness compared to the 5X holes, but this caused increased overall cooling effectiveness, likely due to the increased heat transfer rates in the bore of the cooling hole.

Measurements of the thermal fields above the wall for the X-AOpt and 7-7-7 SI holes are shown in Figure 4.3 for the optimum VR and a high VR for positions of x/D = 2 and 20. Details of these measurements are provided in Yoon et al. (2022). These thermal fields provide insight into how the X-AOpt holes are able to provide much greater adiabatic effectiveness compared to the baseline 7-7-7 SI holes. Immediately obvious in these contour plots is the much broader extent of the coolant distribution for the X-AOpt holes at x/D = 2. This is due not only to a broader exit of these holes, but also to the strong counter rotating vortices generated by the protrusions push the center of the coolant jets towards the surface. Further downstream at x/D = 20, the dramatic improvement in adiabatic effectiveness for the X-AOpt hole is seen to be due to the coolant remaining much closer to the surface and hence with less dispersion of the coolant.

The effects of internal rib turbulators and external TBC (thermal barrier coatings) are presented in Horner et al. (2022). For the rib turbulator study, V-shaped ribs, with a rib height to channel height ratio of 0.25, were placed in the internal coolant channel upstream and

downstream of a row of 15-15-1 RI film cooling holes. These rib turbulators were designed to provide a 3x increase in Nusselt number for the internal coolant flow. The laterally averaged overall cooling effectiveness, $\bar{\phi}$, for the smooth and rib turbulator walls are presented in Fig. 4.4 for film cooling cases with VR = 0.7 to 3.0, and for reference with no film cooling. As expected, $\bar{\phi}$ increases significantly when the rib turbulators are used, with a 50% increase for the no film cooling case. Maximum values of $\bar{\phi}$ occurred at VR = 1.7 with values ranging from $\bar{\phi}$ = 0.5 to 0.43 over the range from x/D = 5 to 40.

To evaluate the effects of TBC, the test plate covered with a simulated TBC which had the same TBC/wall thickness ratio and thermal conductivity ratio as is typical for engine conditions. Measurements of the "metal" surface temperature were made with an array of thermocouples on the Corian surface beneath the simulated TBC, which allowed determination of the overall cooling effectiveness with TBC. Results from these experiments are shown in Fig. 4.5 for smooth and turbulated internal coolant channels with no film cooling and with film cooling with varying VR. With no film cooling, for the smooth wall $\bar{\phi}$ = 0.47 while for the wall with rib turbulators $\bar{\phi}$ = 0.61, i.e. nominally 2x the values measured without TBC. With film cooling, the average overall cooling effectiveness over the range x/D = 10 to 30 was $\bar{\phi}$ = 0.62 for the smooth wall compared to $\bar{\phi}$ = 0.67 for the wall with rib turbulators. Although film cooling still improves the overall cooling effectiveness when TBC is used, the percentage increase is much smaller.

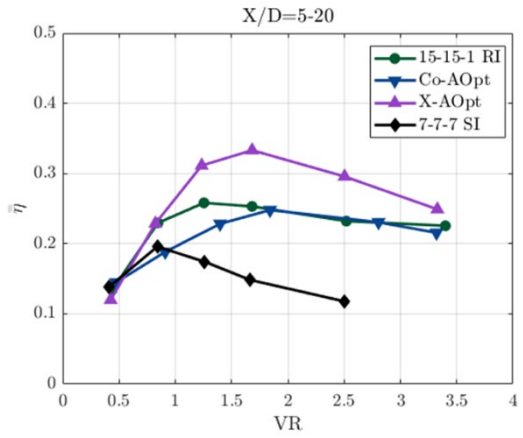

Figure 4.1. Spatially averaged adiabatic effectiveness for the X-AOpt and Co-AOpt, 15-15-1 RI, and 7-7-7 SI holes.

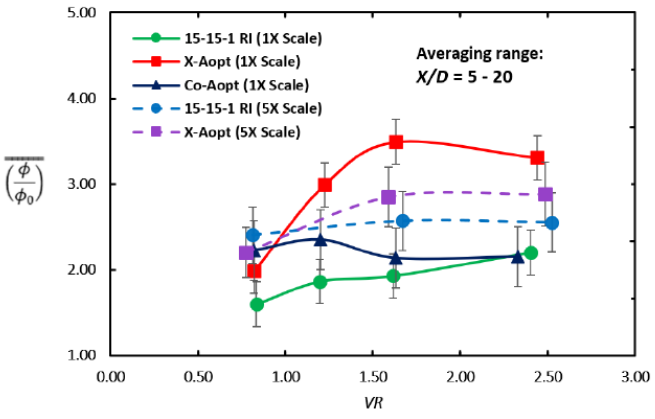

Figure 4.2. Overall cooling augmentation for the X-AOpt and Co-AOpt, and 15-15-1 RI holes for X1 and X5 models.

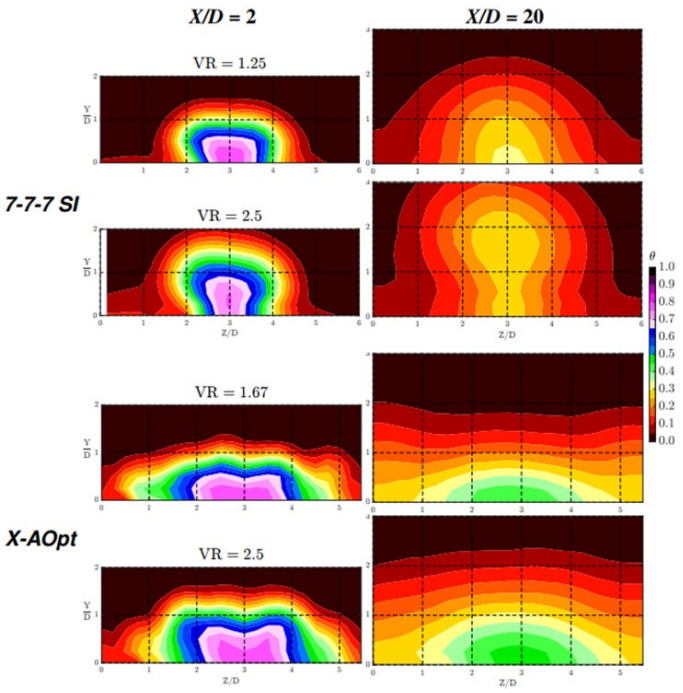

Figure 4.3. Thermal field profiles for the X-AOpt and 7-7-7 SI holes with the optimum *VR* for each hole and a maximum *VR* = 2.5.

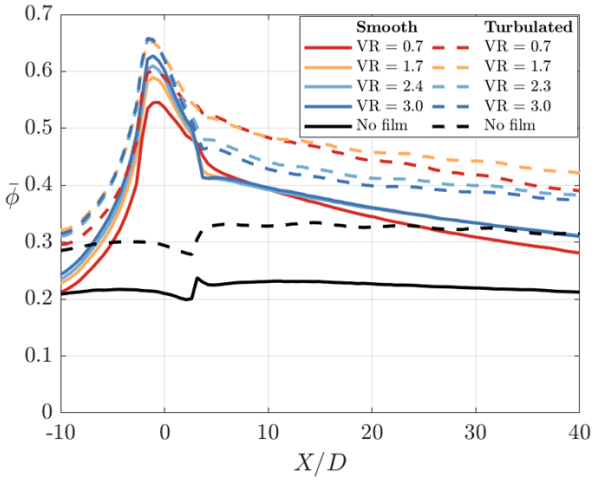

Figure 4.4. Overall cooling effectiveness for the 15-15-1 RI hole with a smooth and a turbulated internal channel.

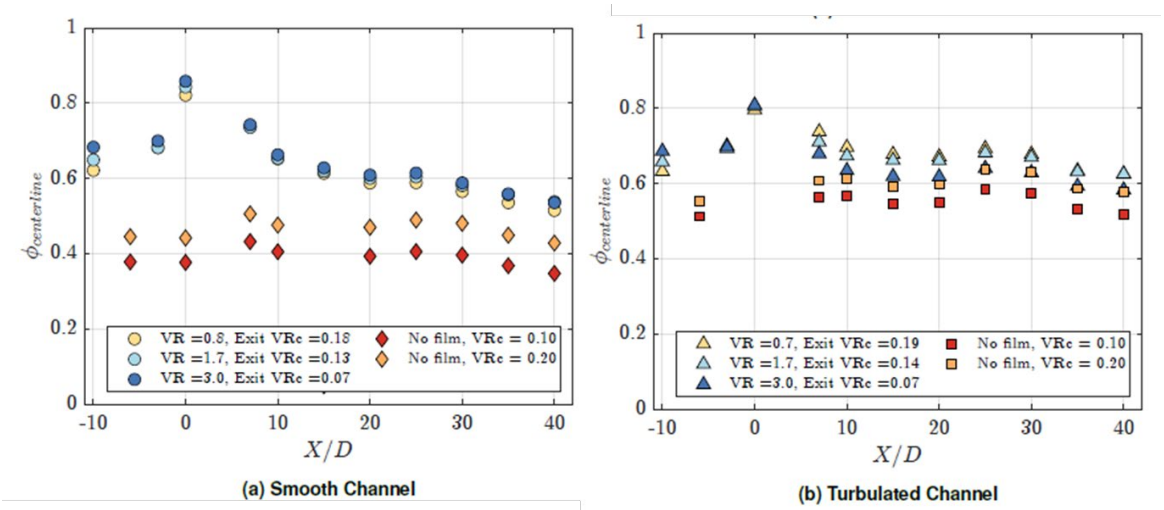

Figure 4.5. Overall cooling effectiveness for the 15-15-1 RI hole with a smooth and a turbulated internal channel and TBC. No film cooling and film cooling cases.

Task 5 (PSU) – Integrate optimal cooling design into the Penn State common turbine vane.

The chosen test article for this project was Penn State's National Experimental Turbine (NExT) vane. This integration and the results are given by Gailey, et al., 2024. The original NExT vane design features four pressure side rows of laidback fan shaped 7-7-7 cooling holes fed from an internally ribbed serpentine passage as illustrated in Figure 5.1. Vane cooling was fed from a plenum at the annulus's outer diameter and flowed radially through the vane to the inner diameter of the annulus. Therefore, the internal cooling flow was a 90° cross-flow to the main gas path (MGP). Coolant was provided to the middle and trailing edge region, while the leading edge had a separately controlled flowrate held at a constant temperature and pressure throughout testing. The specific passage with the film-cooling holes of interest for this study allowed for independently controlled flows, which were varied.

Schematics of the as-designed 7-7-7, 15-15-1, and X-AOpt hole configurations are shown in Figure 5.2(a-c). For the specially designed NExT vane, the first row (Row 1 in Figure 5.1) of cooling holes on the pressure side were chosen to be replaced with the parametrically optimized 15-15-1 [4] and the X-AOpt adjoint optimized [5] holes. It should be noted that the second row (Row 2 Figure 5.1) was designed to be 7-7-7 holes and remained as such for this study. The major difference between the 15-15-1 holes and the X-AOpt holes is the addition of non-symmetric vortex generating bumps on the external surface. These bumps were shown to reverse the counter-rotating vortex created by the cooling hole and push the coolant down onto the surface.

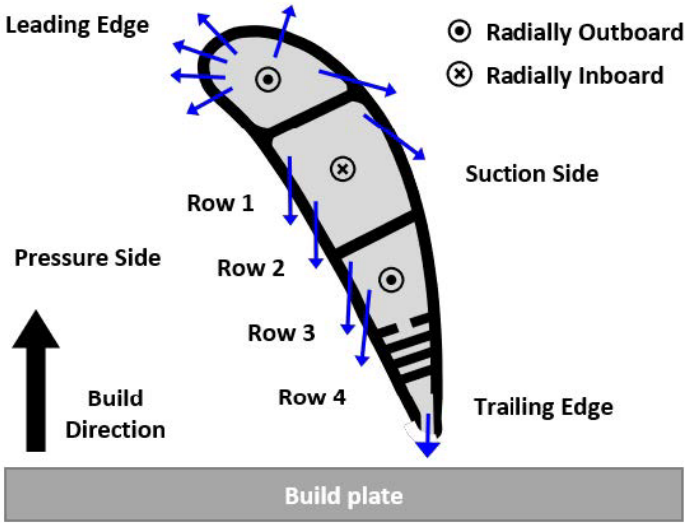

Figure 5.1. NExT vane cartoon indicating Row 1 and Row 2 on the pressure side for evaluating the new cooling holes. Also indicated is the build orientation for additive manufacturing.

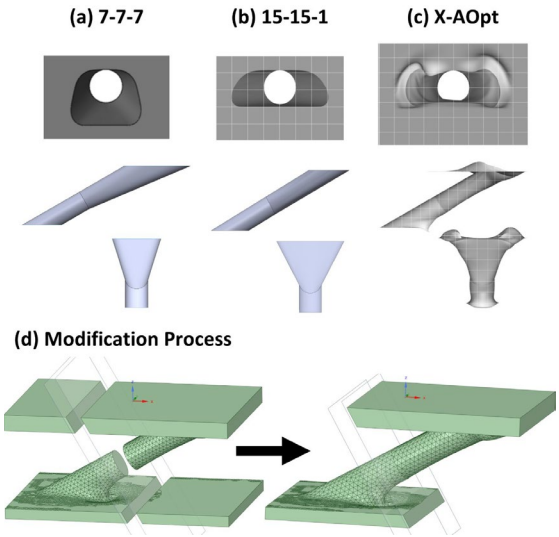

Figure 5.2. Views of the hole wall surface looking down the bore of each cooling hole, from the side, and from downstream looking back towards the hole, top to bottom respectively, for the (a) 7-7-7 (b) 15-15-1 (c) X-AOpt cooling holes and (d) the modification process used.

Task 6 (UT) – Design and testing of a serpentine channel for internal cooling integrated with the optimum film cooling hole.

The proposed original task, which was to test the optimum film cooling hole in a cascade facility, was modified to focus on integrating internal cooling with a serpentine channel with the optimum film cooling geometry. Although serpentine channels are commonly used for the internal cooling of turbine blades, there were no studies in the open literature about the performance of film cooling holes when supplied from a serpentine channel. The flat plate wind tunnel facility was modified to incorporate a serpentine channel, shown schematically in Fig. 6.1, below the test surface. Computational analysis was used to design the serpentine channel with particular attention to angled rib turbulators and the associated pressure losses and heat transfer enhancements. This was followed by experimental verification of the performance of the serpentine channel. Details of this study are available in Yoon et al. (2023 a), with the main highlights presented below.

Computational predictions and experimental measurements were made for rib turbulators with varying rib heights and angles. There were two unexpected results from these studies: the optimum orientation angle was opposite than that typically used and enhancement of heat transfer by rib turbulators in the serpentine channel was much less than obtained in straight channels. Measurements and computational predictions of the pressure drop in the serpentine channel for a smooth channel and various rib configurations are shown in Fig. 6.2. The rib heights used in this study were e/H = 0.125 and 0.25 for the 1X and 2X ribs, respectively. The rib orientations were ± 60° relative to the flow direction. The +60° direction is what is typically used in most turbine cooling designs because the ribs are orient to direct flow towards the inner wall where flow separation occurs. This orientation would naturally be presumed to minimize the separation region and reduce pressure loss. However, as Fig. 6.2 shows, our computational and experimental results showed the -60° rib orientation had much less pressure loss than the +60° orientation. The computational predictions showed that this occurred because the -+60° rib orientation caused a strong rotational flow that induced high speed flow from the opposite wall of the coolant channel towards the inner wall, thereby reducing the separation region.

The effectiveness of the rib turbulators in enhancing heat transfer was quantified by measuring the overall cooling effectiveness with only internal cooling, $\bar{\bar{\phi}}_0$. Experimental results are shown in Fig. 6.3 for the serpentine channel and a coflow channel with varying coolant mass flow rates. These results show that for the coflow channel, the rib turbulators caused as much as a 50% increase in $\bar{\bar{\phi}}_0$, but for the serpentine channel, there was essentially no enhancement in heat transfer with the rib turbulators. We attribute the lack of increase in overall cooling effectiveness for the serpentine channel with rib turbulators to the very high turbulence levels caused by the U-bends in the serpentine channel, which would greatly increase heat transfer for the smooth wall case.

Film cooling experiments were conducted with the serpentine channel using the X-AOpt holes and 7-7-7 SI holes. Details from this study are presented in Yoon et al. (2023 b). Adiabatic effectiveness was measured for a range of $VR = 0.4$ to 2.5 with a channel velocity ratio of $VR_c = 0.4$ with results presented in terms of spatially averaged adiabatic effectiveness, $\bar{\bar{\eta}}$, in Fig. 6.4. For comparison, also presented in Fig. 6.4 are $\bar{\bar{\eta}}$ values for the X-AOpt and 7-7-7 SI holes fed with co-flow and counter-flow channels. As shown in this figure, the performance of the X-AOpt hole was significantly affected by the coolant channel configuration, with the maximum $\bar{\bar{\eta}}$ values for co-flow and counter-flow channels being about 20% larger than the serpentine channel. However, for $VR < 1$, the performance was essentially the same for all three channels. Note that the adiabatic effectiveness for the X-AOpt holes were still significantly larger than the 7-7-7 SI holes for $VR > 1$ for all channels. Measurements of the spatially averaged overall cooling effectiveness, $\bar{\bar{\phi}}$, for the X-AOpt and 7-7-7 SI holes fed with the serpentine channel are presented in Fig. 6.5. The maximum overall cooling effective for the X-AOpt holes was $\bar{\bar{\phi}} \approx 0.55$ which was substantially larger than the $\bar{\bar{\phi}} \approx 0.4$ value for the 7-7-7 SI holes.

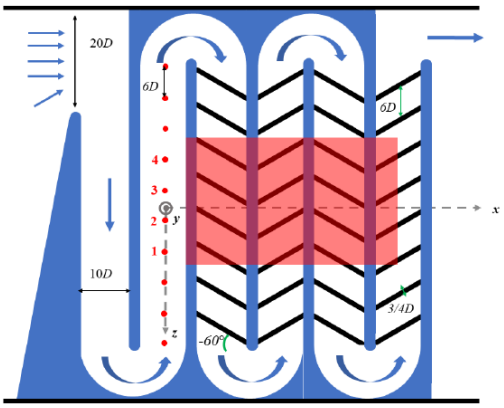

Figure 6.1. Schematic of serpentine channel configuration with -60 ° ribs

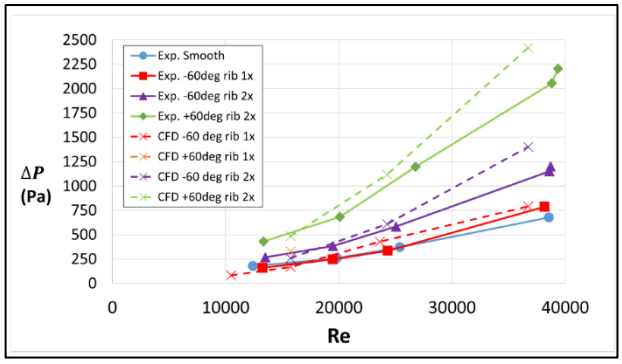

Figure 6.2. Total pressure drop along serpentine channel with varying internal flow Re and varying rib configurations. Experimental and computational results shown.

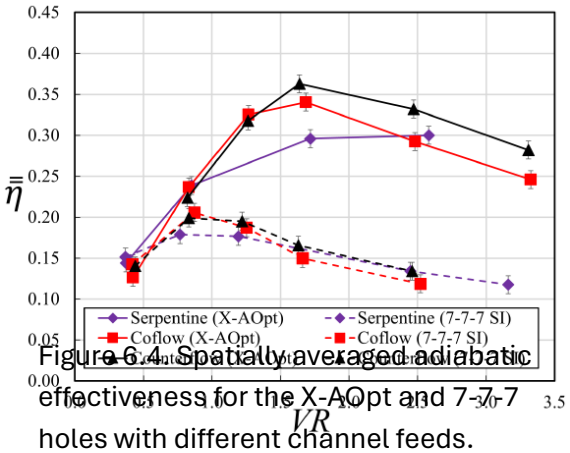

Figure 6.4. Spatially averaged adiabatic effectiveness for the X-AOpt and 7-7-7 holes with different channel feeds.

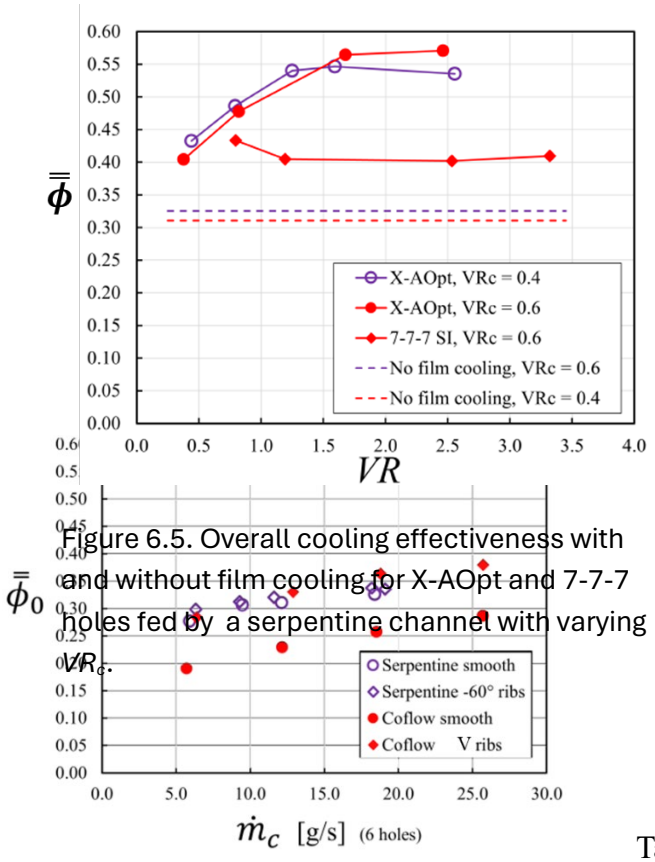

Figure 6.3. Overall cooling effectiveness with no film cooling for serpentine and co-flow coolant channels.

Figure 6.5. Overall cooling effectiveness with and without film cooling for X-AOpt and 7-7-7 holes fed by a serpentine channel with varying VR_c.

Task 7 (PSU) – Testing of 1X common turbine vane with optimized cooling at simulated engine operating conditions.

Understanding how deviations from the design intent alter the cooling performance is critical when scaling specific cooling features to an actual turbine component. At engine scales, cooling flows can behave differently than large scale testing due to differences in how the coolant is supplied to a specific region and because of realistic manufacturing variabilities (Gailey, et al. 2024). This task was to evaluate the film-cooling technologies discussed throughout this report into true-scale AM coupon testing to the integration into an aero-engine vane doublet manufactured using AM. The integration of these cooling holes were discussed in Task 5.

The internal passage that supplied the cooling holes of interest was also modified from the baseline NExT design, which included exclusively discrete V-shaped ribs. Instead, for this study the ribbed section was split into an as-designed region of discrete V-shaped ribs and a modified region of no ribs (smooth) and discrete angled ribs, as shown in Figure 7.1. The hole groups are defined as follows: i) 15-15-1 supplied by a ribbed channel (15-15-1-R), ii) X-AOpt supplied by a smooth channel (X-AOpt-S), iii) 15-15-1 supplied by a smooth channel (15-15-1-S), and iv) 7-7-7 supplied by a ribbed channel (7-7-7-R). The integration of these modifications and their relative locations is represented by the illustration in Figure 7.1, with the first row of cooling holes having four 15-15-1-R, six X-AOpt-S, and then four 15-15-1-S holes progressing from outer span to inner span. Row 2 also consisted of fourteen 7-7-7-R holes radially offset to be

centered between internally adjacent ribs. For this paper, the Row 2 7-7-7-R cooling holes were divided into respective quantities of four, six, and four to match the relative radial locations of the upstream Row 1 hole groups, and are labeled as group 1 (7-7-7-R1), group 2 (7-7-7-R2), and group 3 (7-7-7-R3).

In terms of the best performance, it can be seen in Figure 7.2(a) that the overall effectiveness measurements from the 1X coupon are the same between hole types, while the adiabatic effectiveness for the X-AOpt holes outperforms the 15-15-1 holes for the 5X tests across the streamwise range of X/D= -3 to 4. Gutierrez et al. (2023) did show significant cooling benefits of their X-AOpt hole using their 5X model, which was in part because of the high adiabatic effectiveness levels measured further downstream of their injection location. By including the additional streamwise distance, their results indicated that the X-AOpt hole outperformed the others. In contrast, the 1X and vane results, when focused on the near-hole region, are highly affected by the convective hole cooling. Because the X-AOpt was optimized from the 15-15-1 hole, the upstream metered section and initial diffuser shape provided similar cooling contributions within the 1X coupon experiment which lead to the same ϕ between the holes. This result demonstrates the importance of using the correct material to capture convective effects from the hole cooling and any protrusions into the MGP.

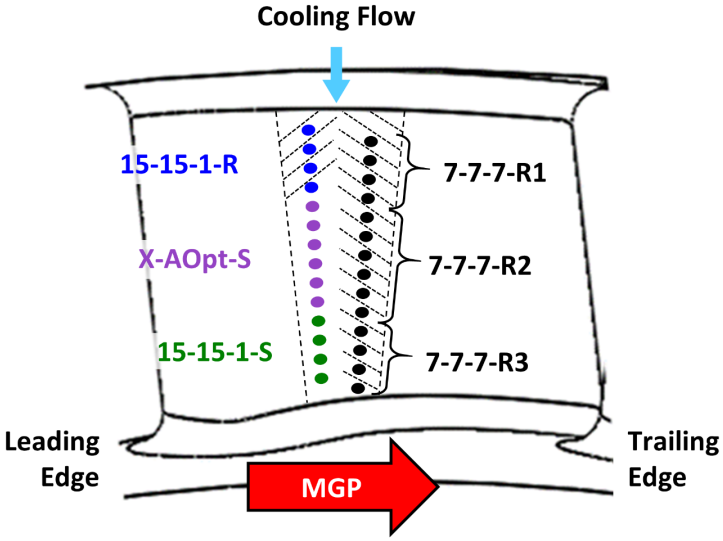

Figure 7.1 The modified NExT vane with integrated cooling holes.

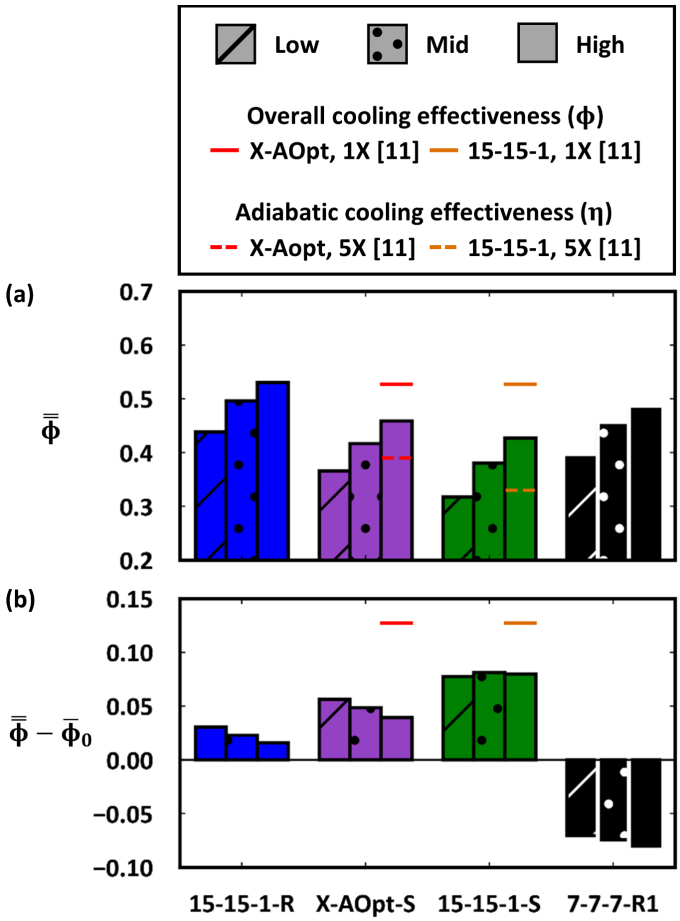

Figure 7.2. (a) Area averaged effectiveness compared to a 5X and 1X coupon test and (b) net area averaged effectiveness improvement for each cooling hole group over the range X/D = -3 to 4.

Task 8 (UT) - Optimized film cooling configuration designed to operate at engine realistic Mach numbers.

Recent studies have shown that design and testing of shaped film cooling holes should be done with realistic Mach numbers. To evaluate the Mach number effects on the performance of the X-AOpt hole, engine scale test coupons were 3D printed and tested in a new transonic test facility at UT. Computational predictions were also done to investigate how compressible effects alter the performance of shaped film cooling holes. Details of these studies were published in Fox et al. (2023(a) and 2023(b)).

The transonic wind tunnel facility used for this task, shown schematically in Fig. 8.1, has one test section which incorporates a flat plate coupon in which different film cooling hole geometries can be tested. Experiments were conducted with mainstream Mach numbers of Ma_∞ = 0.25 and 0.5 with a range of blowing ratios of M = 0.5 to 3 using the X-AOpt holes and, for reference, the 7-7-7 SI holes. For these tests the coolant to mainstream stagnation temperature ratio was maintained at $\mathcal{T}^o = 0.83$, i. e. the equivalent of a density ratio of $DR = 1.2$. Results from these experiments are shown in Figure 8.2 in terms of spatially averaged adiabatic effectiveness, $\bar{\bar{\eta}}$, over the range of x/D = 5 to 20. For $M \leq 1$, $\bar{\bar{\eta}}$ values for both hole geometries were the same for Ma_∞ = 0.25 and 0.50, but for $M \geq 2$, the performance with Ma_∞ = 0.50 was significantly degraded compared to the performance with Ma = 0.25. The 7-7-7 SI holes had a 40% decrease in $\bar{\bar{\eta}}$ values while the X-AOpt holes had a 25% decrease. Also shown in Fig. 8.2 are the results from a computational study by Oliver et al. (2019) in which large eddy simulations (LES) were used to predict the film cooling performance of 7-7-7 SI holes when mainstream Mach numbers varied from Ma_∞ = 0.25 and 0.5. The blowing ratio used in these simulations was M = 2.0, and Fig. 4.2 shows that predicted performance was essentially the same as measured values. Contour plots of adiabatic effectiveness presented in Fig. 8.3 for M = 1 and 2 and Ma = 0.25 and 0.50 show that for M = 2 and Ma_∞ = 0.50, the coolant exiting the holes is highly skewed to one side of the hole, resulting in significantly decreased coverage downstream of the hole. This skewness at Ma_∞ = 0.50 was also predicted computationally.

Computational predictions of high Mach number effects on film cooling were done using RANS simulations. Details of this study are presented in Fox et al. (2023(b)). Validation of these RANS predictions was done by making comparisons with the high fidelity LES predictions by Oliver et al. (2019). Fig. 8.4 shows a comparison of the LES and RANS predictions of the Mach number distributions within a 7-7-7 SI film cooling hole for M = 2 and Ma_∞ = 0.25 and 0.5. Although there are noticeable differences between the RANS and LES predictions, the essential elements are the same, including the acceleration to sonic velocity in the throat of the hole near the inlet and a significant separation region in downstream section of the diffuser. One of the important insights from the computational predictions was the recognition that, at high Mach number, there is a significant variation of coolant density across the exit area of a shaped film cooling hole. This is shown in Fig. 8.5 for a constant blowing ratio of M = 1.75 with varying mainstream Mach numbers from Ma = 0.15 to 0.75. For Ma = 0.15, 0.25, and 0.5, the

density ratio of the coolant relative to the mainstream is nominally 1.2 across the exit area. However, for Ma = 0.75, the coolant density ratio varies from DR = 1.0 to 1.35. Consequently, the coolant cannot be characterized in terms of a single density ratio, and interaction with the mainstream is altered compared to the uniform density ratio that occurs at lower Mach numbers.

Computational predictions were also used to predict the effects of varying coolant to mainstream stagnation temperature ratios of $\mathcal{T}^o = 0.83$ and 0.50. Fig. 8.6 shows the distribution of spatially averaged film cooling effectiveness, $\bar{\bar{\eta}}_r$, for the 7-7-7 SI holes scaled with blowing ratio, M, and the coolant to mainstream pressure ratio, P, for Ma_∞ = 0.75. Two important observations evident from this study for film cooling with high mainstream Mach numbers were: a. film effectiveness for vary coolant temperatures scales with P rather than M, and film effectiveness is noticeably higher with lower coolant temperatures.

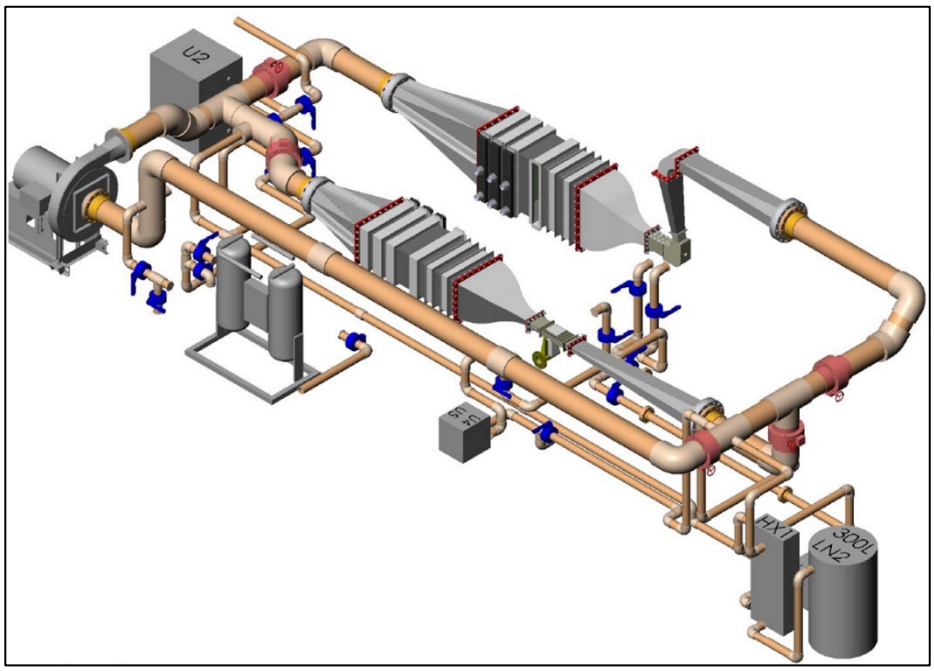

Figure 8.1. Schematic of the transonic wind tunnel facility.

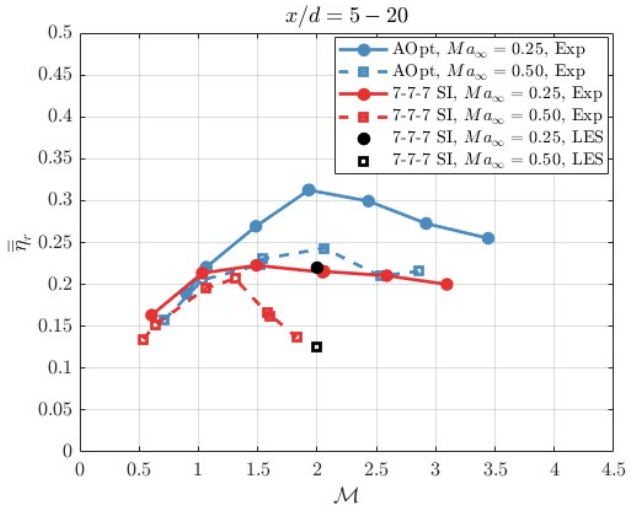

Figure 8.2. Spatially averaged film cooling effectiveness, $\bar{\bar{\eta}}_r$, with varying *M* values for the 7-7-7 SI and the X-AOpt holes. LES data from Oliver et al. (2019).

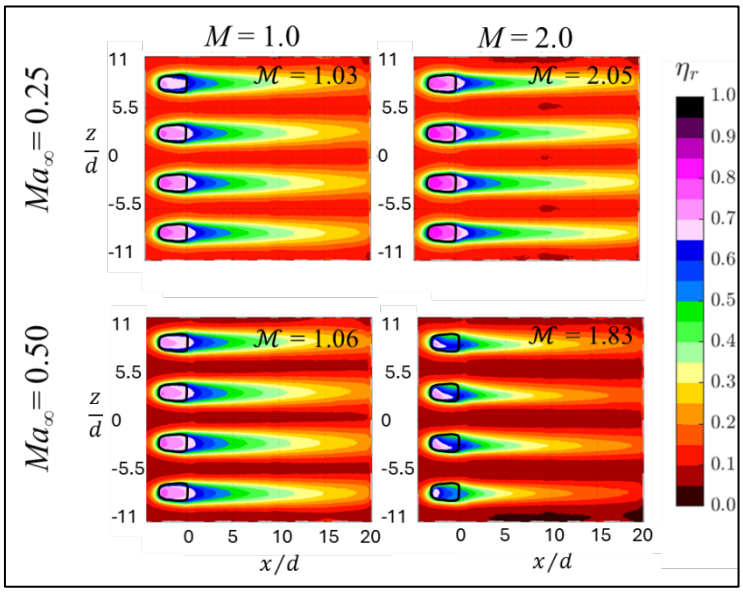

Figure 8.3. Contours of η_r for the 7-7-7 RI hole with varying blowing ratio, *M*, and mainstream Mach number.

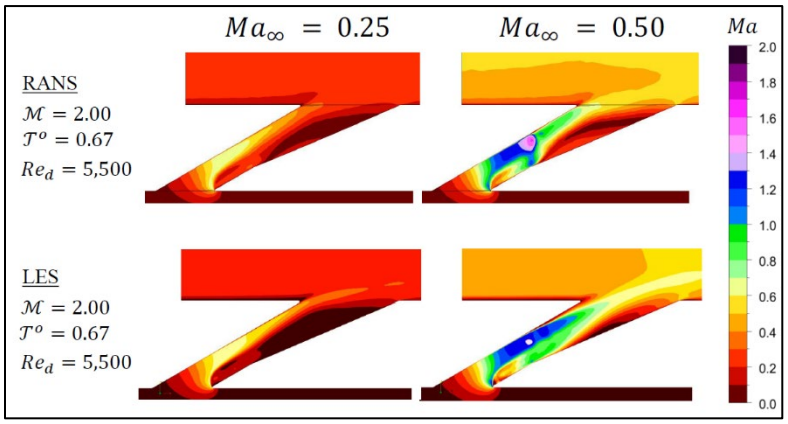

Figure 8.4. Comparison of LES and RANS predictions of in-hole contours of *Ma* for film cooling with 7-7-7 RI holes at *M* = 2.0 and varying mainstream Mach numbers.

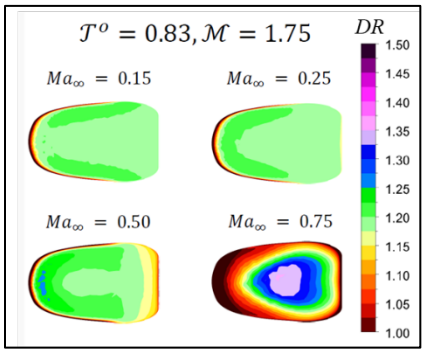

Figure 8.5. Contours of η_r for the 7-7-7 RI hole with varying blowing ratio, *M*, and mainstream Mach number.

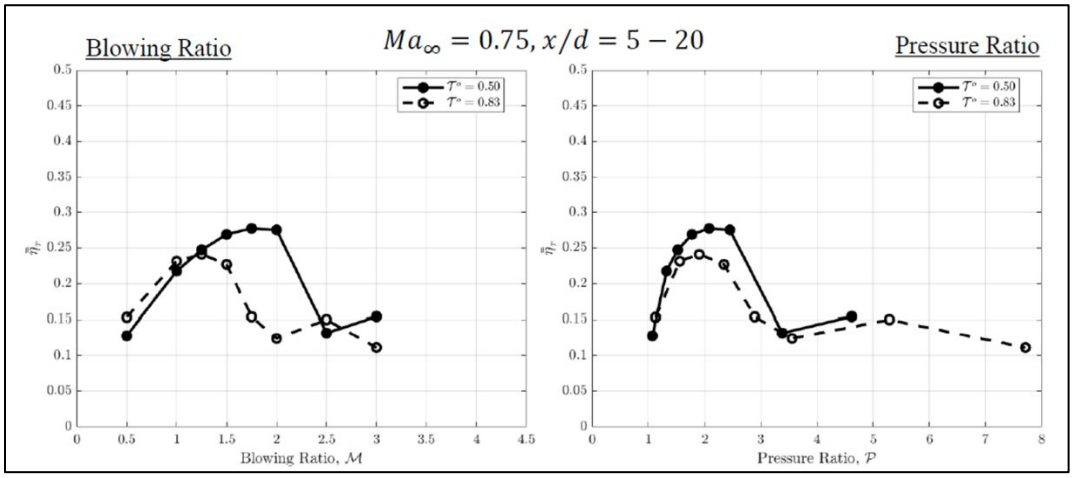

Figure 8.6. Distribution of spatially averaged film cooling effectiveness, $\bar{\bar{\eta}}_r$, for the 7-7-7 SI holes with coolant to mainstream total stagnation temperature ratios of T^o = 0.83 and 0.50 scaled with blowing ratio and pressure ratio.

Task 9 (UT) - Experimental testing of multi-row film cooling configurations simulating the NExT turbine vane.

For this task, the interaction between multiple rows of film cooling holes was studied to determine how film cooling performance was affected by closely spaced film cooling holes. Details of this task were published in Ellinger et al. (2024(a) and 2024(b)). The film cooling hole configurations tested included configurations used on the NExT turbine vane that was tested in the PSU START facility (see Task 7). One objective of this study was to provide insight into the expected performance of the film cooling of the NExT turbine vane. Six multirow film cooling configurations were tested as listed Table 9.1. Configuration B2 simulated two rows of holes on the pressure side of the NExT vane, with the upstream row having X-AOpt holes and the downstream row having 7-7-7 SI holes. Configuration B3 simulated a row of showerhead holes, with 90° compound angle, cylindrical holes. A schematic of the B3 configuration is shown in Figure 9.1. Experiments were conducted using the serpentine channel model for internal cooling. This was similar to the configuration used on the NExT vane model.

Table 9.1. Multirow film cooling configurations with test data generated.

Geometry	Row 1 Hole Geometry	Row 2 Hole Geometry	Row 3 Hole Geometry	η test	Φ test
A2	-	7-7-7 SI	7-7-7 SI	√	
A3	90 deg comp cylindrical	7-7-7 SI	7-7-7 SI	√	√
B2	-	X-AOpt	7-7-7 SI	√	
B3	90 deg comp cylindrical	X-AOpt	7-7-7 SI	√	√
C2	-	X-AOpt	X-Aopt	√	
C3	90 deg comp cylindrical	X-AOpt	X-Aopt	√	

Samples of the measured adiabatic effectiveness distributions are presented in Fig. 9.2 for the A2, B2, and C2 configurations at high velocity ratios of nominally $VR = 2.5$. The B2 configuration had higher η levels than the A2 configuration in the near hole area, but effectiveness levels were similar farther downstream. The C2 configuration had noticeably higher adiabatic effectiveness levels throughout. The laterally averaged adiabatic effectiveness values for these configurations are presented in Fig. 9.3 for nominal velocity ratios of $VR = 1.3$ and 2.5. Also presented in Fig. 9.3 are film cooling performance levels predicted using the Sellers' superposition model. The superposition model predicts performance of multiple rows of film cooling holes based on the measured performance of a single row of holes. Many studies in the literature have shown that the Seller's superposition model provides reasonably accurate predictions for most multirow film cooling configurations. As shown in Fig. 9.3, the superposition model corresponded reasonably well for the A2 configuration, but significantly overpredicted performance for the B2 and C2 configurations. The A2 configuration had two rows of conventional 7-7-7 SI film cooling holes, so reasonable predictions of performance with the superposition model is expected. The overprediction of adiabatic effectiveness for the B2 and C2 configurations can be attributed to the effects on the external vortices generated by the X-AOpt holes by the downstream film cooling holes. These vortices are aligned so that they cause

a downflow on the coolant jet as it exits the hole. However, these vortices were not appropriately position to have this effect on the downstream holes which were staggered with respect to the upstream holes. Consequently, the predicted enhanced performance for the X-AOpt holes did not occur. These results indicate that the performance of the multirow configuration used on the NExT vane, consisting of X-AOpt holes followed by 7-7-7 SI holes, would not show an increased performance relative to that for multiple rows of 7-7-7 SI holes.

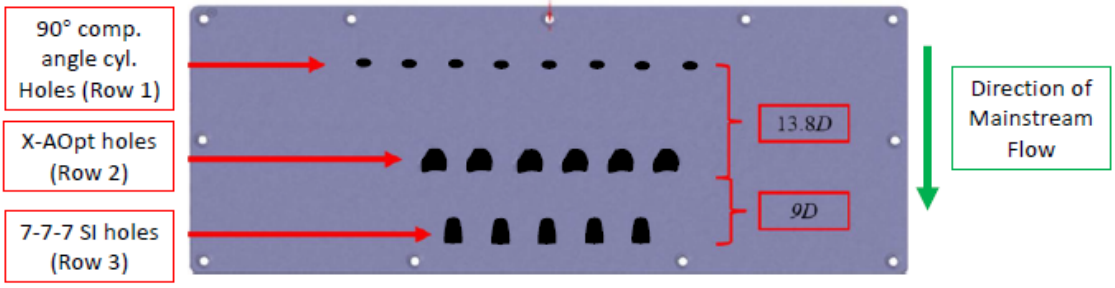

Figure 9.1. Schematic of the B3 coupon used for multirow film cooling testing.

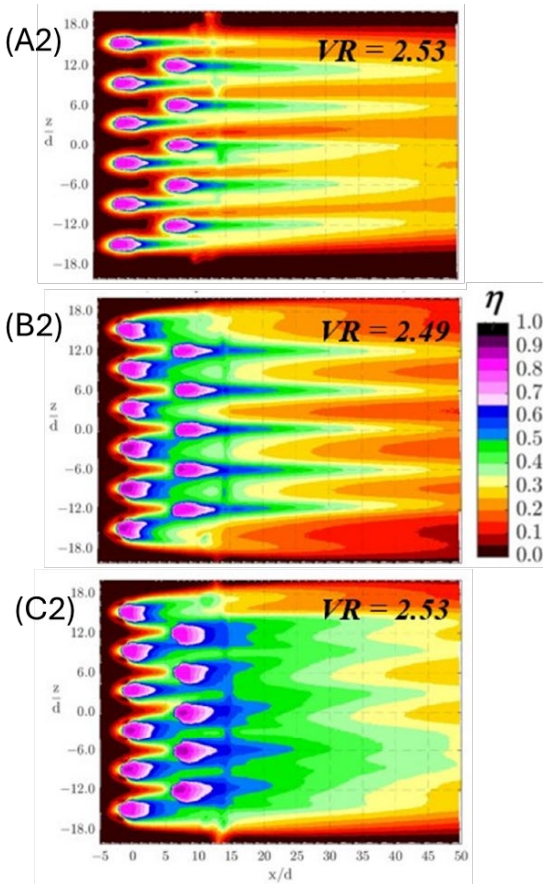

Figure 9.2. Contours of η_r for the A2, B2, and C2 configurations.

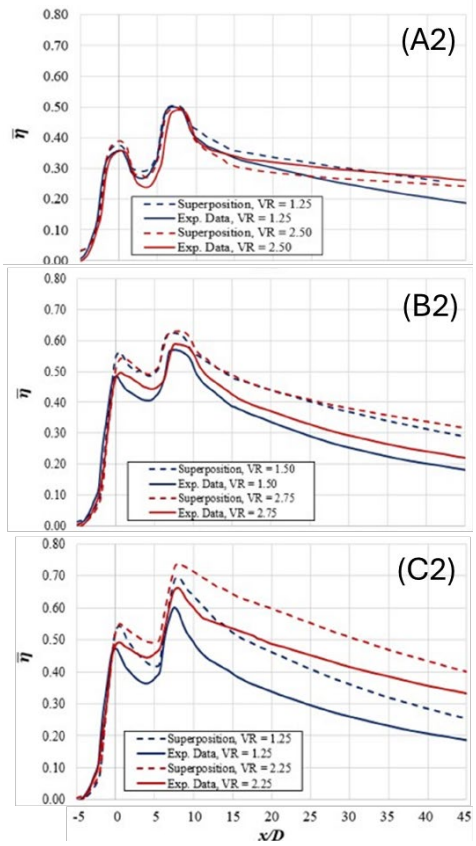

Figure 9.3. Laterally averaged η_r for the A2, B2, and C2 configurations and superposition predictions for each case.

References (Papers generated from work done on this project):

Ellinger, M.E., Flachs, E.M., and Bogard, D.G., 2024, "Investigation of the Effects of Geometry Variations on the Performance of an Adjoint Optimized Film Cooling Hole", GT2024-128042. DOI: 10.1115/GT2024-128042

Ellinger, M.E., Flachs, E.M., Kulkarni, A.N., and Bogard, D.G., 2024, "Evaluation of Superposition Predictions of Adiabatic and Overall Effectiveness for three rows of Film Cooling Holes with Differing Geometries", GT2024-128105. DOI: 10.1115/GT2024-128105

Fox, D.W., Furgeson, M.T., and Bogard, D.G., 2023 (a), "Considerations for Compressible Film Cooling: A Computational Study of the Effects of Transonic Flows and Varying Mainstream Mach Number," ASME Gas Turbine Expo, paper GT2023-104049, Boston, USA, June, 2023. DOI: 10.1115/GT2023-104049

Fox, D.W., Furgeson, M.T., Flachs, E.M., and Bogard, D.G., 2023 (b), "Experimental Study of Compressible Film Cooling Scaling and Hole Geometry," ASME Gas Turbine Expo, paper GT2023-104038, Boston, USA, June, 2023. DOI: 10.1115/GT2023-104038

Furgeson, M.T., Veley, E.M., Yoon, C., Gutierrez, D., Bogard, D.G., and Thole, K.A., 2022, "Development and Evaluation of Shaped Film Cooling Holes Designed for Additive Manufacturing," ASME Gas Turbine Expo, paper GT2022-83201, Rotterdam, Netherlands, June, 2022. DOI: 10.1115/GT2022-83201

Gailey, N., Barringer, M. D., Berdanier, R. A., and Thole, K. A., *Integration of Cooling Holes Into a Turbine Vane Made Using Additive Manufacturing*, GT2024-124085. DOI: 10.1115/GT2024-124085

Gutierrez, D., Yoon, C., Furgeson, M. T., Veley, E., Bogard, D. G., Thole, K. A., 2023, "Evaluation of Adjoint Optimized Holes – Part I Baseline Performance," *Journal of Turbomachinery* DOI: 10.1115/1.4056390

Horner, M.J., Yoon, C., Furgeson, M., Oliver, T.A., and Bogard, D.G., 2022, "Experimental and Computational Investigation of Integrated Internal and Film Cooling Designs Incorporating a Thermal Barrier Coating," *ASME J. Turbomach.*, Vol. 144(9), pp. 091001-1-12, DOI: 10.1115/1.4053723

Jones, F.B., Fox, D.W., Oliver, T.A., and Bogard, D.G., 2021 (a) "Parametric Optimization of Film Cooling Hole Geometry," ASME Turbo Expo Conference, Paper GT2021-59326 Virtual Conference, June. 2021. DOI: 10.1115/GT2021-59326

Jones, F.B., Oliver, T.A., and Bogard, D.G., 2021 (b) "Adjoint Optimization of Film Cooling Hole Geometry," ASME Turbo Expo Conference, Paper GT2021-59332, Virtual Conference, June. 2021. DOI: 10.1115/GT2021-59332

Jones, F.B., Fox, D.W., and Bogard, D.G., 2023, "Experimental and Computational Investigation of Shaped Film Cooling Holes Designed to Minimize Inlet Separation**,"** *ASME J. Turbomach.*, Vol. 145(9), pp. 091007-(10 pages), Sept. 2023, DOI: 10.1115/1.4062460.

Veley, E., Thole, K. A., Furgeson, M. T., Bogard, D. G., 2023, "Printability and Overall Cooling Performance of Additive Manufactured Holes with Inlet and Exit Rounding," *Journal of Turbomachinery*, vol. 145 (3), pp. 031017. DOI: 10.1115/1.4056389

Veley, E. and Thole, K. A., 2023, "Cooling Performance of Film-Cooling Holes Fed by Channels of Various Shapes", *International Journal of Heat and Mass Transfer,* vol. 216, pp. 124561.

Veley, E. Thole, K. A., and Bogard, D. G., 2024, "The Effects of Channel Supplies on Overall Film-Cooling Effectiveness", *J of Turbomachinery,* vol. 146 (3), pp. 031006. DOI: 10.1115/1.4063927

Wildgoose, A. and Thole, K. A., 2023, "Heat Transfer and Pressure Loss of Additively Manufactured Internal Cooling Channels with Various Shapes," *Journal of Turbomachinery* vol. 145(7), pp. 071011. DOI: 10.1115/1.4056775

Yoon, C., Gutierrez, D., Furgeson, M.T., and Bogard, D.G., 2022, "Evaluation of Adjoint Optimized Hole – Part II: Parameter Effects on Performance," ASME Gas Turbine Expo, paper GT2022-82726, Rotterdam, Netherlands, June, 2022. DOI: 10.1115/GT2022-82726

Yoon, C., Flachs, E.M., Ellinger, M.E., Bogard, D.G., 2023 (a), "Overall Cooling Effectiveness with Internal Serpentine Channels and Optimized Film Cooling Holes," ASME Gas Turbine Expo, paper GT2023-104171, Boston, USA, June, 2023. DOI: 10.1115/GT2023-104171

Yoon, C., Ellinger, M.E., Bogard, D.G., 2023 (b) "Evaluation of Pressure Drop and Cooling Effectiveness of Serpentine Channels with Varying Internal Rib Configurations," ASME Gas Turbine Expo, paper GT2023-104216, Boston, USA, June, 2023. DOI: 10.1115/GT2023-104216